

## BUOYANCY-DRIVEN FLOW AND FORCED FLOW OF COMPLEX FLUID WITHIN A TRIANGULAR CHAMBER WITH A ROTATING BODY

Youcef LAKAHAL\*, Housseem LAIDOUDI\*

\*Faculty of Mechanical Engineering, University of Sciences and Technology of Oran, BP 1505, El -Menaouer, Oran 31000, Algeria

[housseem.laidoudi@univ-usto.dz](mailto:housseem.laidoudi@univ-usto.dz), [youcef.lakahal@univ-usto.dz](mailto:youcef.lakahal@univ-usto.dz)

*received 13 October 2024, revised 26 January 2025, accepted 10 February 2025*

**Abstract:** This study investigates mixed convection heat transfer of a non-Newtonian fluid within a finned triangular cavity containing a horizontally oriented, rotating cylinder with a circular cross-section. The cylinder, maintained at a high temperature, rotates at a constant speed, while the cavity walls are kept at a cold temperature. This configuration is significant for applications in cooling technologies and materials processing. Unlike previous studies that primarily focused on simpler geometries, this work uniquely examines the effects of varying blockage ratios in a finned triangular cavity, a less explored configuration. The analysis considers key parameters such as cylinder rotation speed ( $Re = 1, 5, \text{ and } 10$ ), thermal buoyancy intensity ( $Ri = 0, 1, 2, \text{ and } 3$ ), fluid viscosity (characterized by the power-law index,  $n=0.6, 1, \text{ and } 1.6$ ), and blockage ratio ( $\beta = 0.12, 0.24, \text{ and } 0.36$ ). Numerical simulations were performed using the finite volume method to solve the governing equations, with Ostwald's law modeling the fluid's rheological properties. Results show that increasing the blockage ratio stabilizes the flow, suppressing counter-rotating regions around the cylinder and reducing the heat transfer rate by more than 30%. Additionally, a decrease in the fluid's power-law index enhances heat transfer from the hot cylinder. These findings provide valuable insights for optimizing thermal systems.

**Key words:** Complex fluid, mixed convection, blockage ratio, numerical investigation, Nusselt number, CFD

### 1. INTRODUCTION

Heat transfer in fluids with complex rheological properties is a growing area of research due to its critical role in industrial applications such as energy storage, cooling technologies, and material processing. Non-Newtonian fluids, particularly those with power-law characteristics, exhibit unique thermal and flow behaviors, making them essential for optimizing engineering systems. Mixed convection, which combines forced and natural convection effects, is especially significant in systems with confined geometries and rotating components.

Numerous studies have advanced our understanding of non-Newtonian fluid dynamics and heat transfer. For instance, laminar forced convection around two heated cylinders in a square duct has shown that cylinder spacing and the power-law index significantly affect flow structure [1]. Pore-scale simulations using the thermal lattice Boltzmann method have demonstrated that porosity and permeability enhance thermal conductivity in porous structures [2]. Natural convection in trapezoidal enclosures has revealed that geometry influences heat transfer, with the aspect ratio affecting temperature distribution and flow patterns [3]. Studies of magnetohydrodynamic (MHD) double-diffusive natural convection in crown enclosures have highlighted the role of magnetic fields in altering flow structure and improving heat transfer [4]. Additionally, investigations of natural convection in shallow horizontal rectangular cavities heated from below have shown that the Nusselt number increases with the power-law index as buoyancy forces dominate [5].

Research on vertical cavities subjected to horizontal temperature gradients indicates that increasing temperature differences

enhances heat transfer rates [6]. Mixed convection in lid-driven square cavities has demonstrated that thermal performance varies significantly with the interaction between fluid motion and the moving lid [7]. Similarly, studies of mixed convective heat transfer in square enclosures using higher-order finite element methods emphasize that heat transfer strongly depends on the flow regime and enclosure geometry [8]. Other work on mixed convection of non-Newtonian fluids in square chambers with discrete heating configurations highlights the impact of heating arrangements on flow and thermal performance [9].

Investigations into specific configurations have also provided valuable insights. For example, double-diffusive effects in Casson fluid flow past wavy inclined plates have shown how temperature and concentration gradients influence heat transfer [10]. Skewed lid-driven cavities have been found to enhance convective heat transfer under certain conditions [11]. Studies of power-law fluids and magnetic fields in staggered porous cavities have revealed a significant reduction in heat transfer rates when these factors are combined [12]. The arrangement of cylinders in flow fields has been shown to critically affect heat transfer efficiency [13]. Furthermore, hybrid nanofluids in 3D lid-driven chambers under magnetic fields have demonstrated improved thermal performance and reduced entropy generation [14]. Finally, research on tandem circular cylinders in cross-flow at low Reynolds numbers has indicated that proximity significantly affects flow patterns and heat transfer [15].

Nanofluids, with their enhanced thermal properties due to nanoparticle inclusion, have also been extensively studied. The role of curved fins in shaping flow patterns and analyzing entropy generation in buoyancy-driven magnetized hybrid nanofluid transport

has been investigated, offering insights into thermal management [16]. Magnetically driven hybrid nanofluid transport in micro-wavy channels has demonstrated potential applications in MEMS-based drug delivery systems [17]. Studies on buoyancy-driven magnetized hybrid nanofluids in discretely heated circular chambers with fins have shown the importance of heat source configurations on hydrothermal performance [18].

Further research on natural convection and MHD effects in alumina nanofluids within triangular enclosures equipped with fins has emphasized the role of geometry in enhancing heat transfer performance [19]. Investigations into thermal modes of obstacles within triangular cavities have advanced the understanding of  $Al_2O_3$ -water nanofluid transport mechanisms [20]. Similarly, buoyancy-driven MHD hybrid nanofluid flow in circular enclosures with fins has provided strategies for optimizing heat transfer in complex systems [21].

The development of numerical methods has further enriched this field. Studies on nanofluid convection heat transfer in renewable energy systems have highlighted its potential to improve energy efficiency [22]. The interaction of magnetic fields with heat transfer processes has been explored, shedding light on convection under MHD conditions [23]. Research on cavity design has emphasized its critical role in optimizing heat transfer performance [24]. The effects of heat source placement on natural convection in enclosures have also been examined, offering strategies to enhance thermal management [25]. Additionally, the thermal behavior of complex systems influenced by cavity design has been thoroughly investigated [26].

Despite these advances, the study of mixed convection in non-Newtonian fluids within finned triangular cavities remains underexplored, particularly in the presence of rotating cylinders. Fins are widely used in engineering systems, such as heat exchangers and cooling devices, to enhance thermal performance by increasing surface area and influencing flow behavior. Previous studies have demonstrated that fins significantly improve heat transfer and flow dynamics in buoyancy-driven and mixed convection systems [27].

Building on these insights, the current study investigates the effects of mixed convection in a finned triangular cavity containing a horizontally oriented, rotating cylinder. The analysis focuses on the effects of blockage ratio ( $\beta = d/L$ ), Reynolds and Richardson numbers, and the rheological properties of power-law fluids on flow and heat transfer. Numerical simulations, conducted using the finite volume method, provide detailed insights into the interaction of these parameters, contributing to the optimization of energy storage systems, cooling technologies, and industrial processes. By integrating and expanding existing knowledge, this study bridges gaps in the literature and offers a novel perspective on mixed convection in power-law fluids, laying a foundation for future advancements in thermal management.

## 2. PHYSICAL PROBLEM AND MATHEMATICAL FORMULATIONS

Fig. 1 illustrates the computational domain used for this investigation. It consists of a rotating horizontal cylinder inside a finned triangular cavity.

The ratio of cylinder diameter  $d$  to the side length of the triangular cavity  $L$  defines the blockage ratio ( $\beta = d/L$ ), it takes three values,  $\beta = 0.12, 0.24$  and  $0.36$ . The cylinder has a hot temperature  $T_h$  and rotates in a counterclockwise direction ( $\Omega$ ), while the triangular cavity remains at a cold temperature  $T_c$  ( $T_h > T_c$ ). The space

between the cylinder and the triangular cavity is assumed to be filled with power law fluids. Three values of the power-law index ( $n$ ) were considered ( $= 0.6, 1$  and  $1.6$ ).

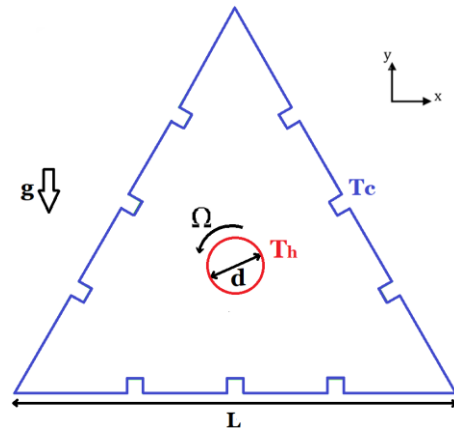


Fig. 1. Diagrammatic representation of the problem

Mixed convection occurs when both natural and forced convection mechanisms are involved in heat transfer. In this study, the rotation of the cylinder generates forced convection, while the temperature difference between the cylinder's surface and the cavity drives natural convection. The Reynolds number controls the rotational speed of the cylinder, while the Richardson number defines the relative contribution of forced versus natural convection. Four Richardson numbers are considered: 0, 1, 2, and 3.

The assumptions of laminar and non-Newtonian flow, steady-state conditions, mixed convection, and constant fluid properties are adopted in this study. The equations of continuity, momentum, and energy, subject to the Boussinesq approximation and neglecting dissipation effects, are first presented in their dimensional form as follows [1]:

The equation of continuity:

$$\frac{\partial u}{\partial x} + \frac{\partial v}{\partial y} = 0 \quad (1)$$

The equation of momentum along the x-direction:

$$\frac{\partial(uu)}{\partial x} + \frac{\partial(uv)}{\partial y} = -\frac{\partial p}{\partial x} + \left( \frac{\partial \tau_{xx}}{\partial x} + \frac{\partial \tau_{yx}}{\partial y} \right) \quad (2)$$

The equation of momentum along the y-direction:

$$\frac{\partial(uv)}{\partial x} + \frac{\partial(vv)}{\partial y} = -\frac{\partial p}{\partial y} + \left( \frac{\partial \tau_{xy}}{\partial x} + \frac{\partial \tau_{yy}}{\partial y} \right) \quad (3)$$

The equation of energy:

$$\rho C_p \left( u \frac{\partial T}{\partial x} + v \frac{\partial T}{\partial y} \right) = k \left( \frac{\partial^2 T}{\partial x^2} + \frac{\partial^2 T}{\partial y^2} \right) \quad (4)$$

To generalize the analysis, these equations are rewritten in dimensionless form using the dimensionless variables [28]:

The equation of continuity:

$$\frac{\partial u^*}{\partial x^*} + \frac{\partial v^*}{\partial y^*} = 0 \quad (5)$$

The equation of momentum along the x-direction:

$$u^* \left( \frac{\partial u^*}{\partial x^*} \right) + v^* \left( \frac{\partial u^*}{\partial y^*} \right) = -\frac{\partial p^*}{\partial x^*} + \frac{1}{Re} \left( \frac{\partial \tau_{xx}^*}{\partial x^*} + \frac{\partial \tau_{yx}^*}{\partial y^*} \right) \quad (6)$$

The equation of momentum along the y-direction:

$$u^* \left( \frac{\partial v^*}{\partial x^*} \right) + v^* \left( \frac{\partial v^*}{\partial y^*} \right) = -\frac{\partial p^*}{\partial y^*} + \frac{1}{Re} \left( \frac{\partial^2 v^*}{\partial x^{*2}} + \frac{\partial^2 v^*}{\partial y^{*2}} \right) + Ri \times T^* \quad (7)$$

The equation of energy:

$$u^* \left( \frac{\partial T^*}{\partial x^*} \right) + v^* \left( \frac{\partial T^*}{\partial y^*} \right) = \frac{1}{Pe} \left( \frac{\partial^2 T^*}{\partial x^{*2}} + \frac{\partial^2 T^*}{\partial y^{*2}} \right) \quad (8)$$

Re and Pe are the Reynolds and Peclet numbers, Ri is the Richardson number, and  $u^*$  and  $v^*$  are the fluid dimensionless velocities in the  $x^*$  and  $y^*$  directions. Dimensionless pressure and temperature are represented by the numbers  $p^*$  and  $T^*$ , respectively. The following represents the dimensionless variables [28]:

$$x^* = x/d, y^* = y/d, u^* = u/(\Omega \times d), \text{ and } v^* = v/(\Omega \times d) \quad (9)$$

$$p^* = p/\rho(\Omega \times d)^2, T^* = (T - T_c)/(T_h - T_c) \quad (10)$$

$$Pe = Re \times Pr \quad (11)$$

The following equation represents the power-law fluid's behavior [28]:

$$\tau_{ij} = 2\eta \varepsilon_{ij} \quad (12)$$

where the viscous stress tensors and the rate of deformation are represented, respectively, by  $\varepsilon_{ij}$  and  $\tau_{ij}$ . Furthermore, for power-law fluids, the fluid viscosity, denoted by  $\eta$ , is defined (in dimensional form) as follows [28]:

$$\eta = m \left( \frac{I_2}{2} \right)^{\frac{n-1}{2}} \quad (13)$$

where  $I_2$  is the second invariant of the rate of deformation tensor,  $m$  is the consistency index, and  $n$  is the power-law index. A fluid that is shear-thinning is represented by  $n < 1$ , a Newtonian limit by  $n = 1$ , and a shear-thickening fluid by  $n > 1$ . The following equation gives  $I_2$  in Cartesian coordinates [28]:

$$\left( \frac{I_2}{2} \right) = 2 \left( \frac{\partial u}{\partial x} \right)^2 + 2 \left( \frac{\partial v}{\partial y} \right)^2 + \left[ \left( \frac{\partial u}{\partial y} \right) + \left( \frac{\partial v}{\partial x} \right) \right]^2 \quad (14)$$

Generally, Grashof number and Richardson number for power law fluids are computed as follows [28]:

$$Gr = g\beta_T \Delta T d^3 \left( \frac{\rho}{m} (\Omega)^{1-n} \right)^2 \quad (15)$$

$$Ri = \frac{g\beta_T \Delta T d^3}{(\Omega \times d)^2} = \frac{Gr}{Re^2} \quad (16)$$

where  $\rho$ ,  $g$ , and  $\beta_T$  are the density of the fluid, the gravitational acceleration and volumetric expansion coefficient, respectively.

The average Nusselt number, or Nu, is calculated by integrating local values along the surface area of the inner cylinder A. The following are Nu's average and local values [28]:

$$Nu_L = \left( \frac{\partial T^*}{\partial n} \right)_{wall}, Nu = \frac{1}{A} \int_s Nu_L dA \quad (17)$$

### 3. NUMERICAL PROCEDURE

The current study was conducted using ANSYS-CFX, a commercial computational fluid dynamics (CFD) software, to

numerically simulate the system. This software converts the governing equations of heat transfer and fluid dynamics into an algebraic form, which are then solved using the finite volume method. For numerical simulations, ANSYS-CFX was employed, utilizing a high-resolution scheme for the convective terms and the SIMPLEX algorithm to handle the pressure-velocity coupling. A calculation error threshold of  $10^{-6}$  was set for both thermal and fluid dynamic equations to ensure convergence accuracy. The mesh required for the simulations was generated using Gambit. After importing the mesh into CFD-Pre, boundary conditions were defined and applied to the problem domain. For visualization and post-processing, including the generation of contour plots, CFD-Post was used to analyze and present the simulation results.

The numerical method employed in this study ensures high accuracy and reliability in solving complex heat transfer and fluid dynamics problems. Using ANSYS-CFX with a high-resolution scheme minimizes numerical diffusion, while the SIMPLEX algorithm provides efficient pressure-velocity coupling. The finite volume method and a convergence criterion of  $10^{-6}$  guarantee solution stability. Unlike analytical methods, which are limited to simplified geometries, this approach handles complex domains and non-linear interactions with flexibility. Additionally, it is less resource-intensive than experimental approaches and allows for comprehensive analysis. The integration of Gambit for mesh generation and CFD-Post for visualization ensures efficient data processing and high-quality results, making the method suitable for diverse engineering applications.

The accuracy of the numerical simulation is strongly influenced by the number of grid elements, making the selection of an optimal mesh density crucial (Fig. 2). A grid independence test was therefore performed to determine the appropriate mesh size, as shown in Table 1. Three different mesh densities were tested, with each mesh used to calculate the Nusselt number for the heated body under conditions of  $n = 1.6$ ,  $Re = 10$ ,  $Ri = 2$  and  $\beta = 0.12$ . The results confirmed that mesh M2 is optimal, as it produced Nusselt values comparable to those of the denser M3, indicating that further refinement would not significantly impact the results.

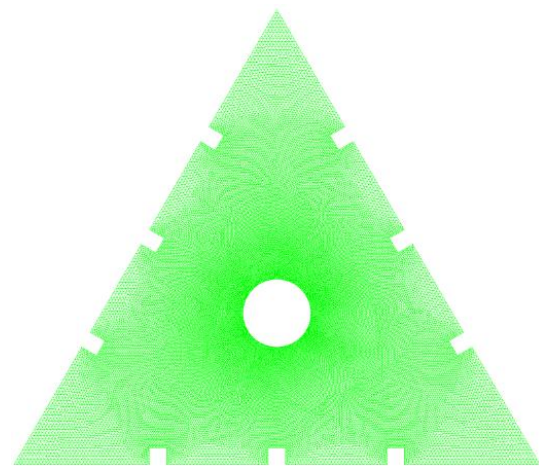


Fig. 2. The structure of the grid used for the calculations

Fig. 3 illustrates the convergence behavior of residuals for the case where  $Re = 5$ ,  $Ri = 0$ ,  $n = 0.6$ , and  $\beta = 0.12$  in the numerical simulation. Fig. 3(A) presents the Root Mean Square (RMS) residuals for mass continuity and velocity components ( $u, v$ ) over

accumulated time steps, while Fig. 3(B) depicts the RMS residual for energy. The residuals exhibit a consistent decrease and stabilize below the convergence threshold of  $10^{-6}$ , confirming successful numerical convergence.

The accuracy of the numerical model has been validated through comparisons with the studies by Kuehn and Goldstein [37] and Matin and Khan [38], which investigated buoyancy-driven flow between two concentric cylinders. Fig. 4(A) illustrates the effect of Rayleigh number ( $Ra = Pr \cdot Gr$ ) on the Nusselt number at  $Pr = 0.71$  and  $n = 1$ , showing a strong agreement between our results and the reference data. So that the maximum value of the difference between the experimental and numerical results is less than 1%. Additionally, a second comparison was conducted to assess the influence of the non-Newtonian behavior of the fluid, specifically the effect of the power-law index  $n$ . For this purpose, results were compared with those of Matin et al. [39], as shown in Fig. 4(B) at  $Pr = 100$  with a blockage ratio of 0.25. The results high-light the impact of the power-law index on the Nusselt number, again confirming good agreement. Fig. 4(C) shows a comparison test between present results and the results of [31]. The results are about the natural convection between two cylinders. Fig. 4(C) presents a good agreement.

Tab. 1. Grid independency test for  $n = 1.6$ ,  $Re = 10$ ,  $Ri = 2$  and  $\beta = 0.12$

Mesh	Elements	Nu	Difference %	CPU Seconds
M1	130,000	3.41930	1.478	622
M2	260,000	3.36876	0.011	1021
M3	520,000	3.36913	-	-

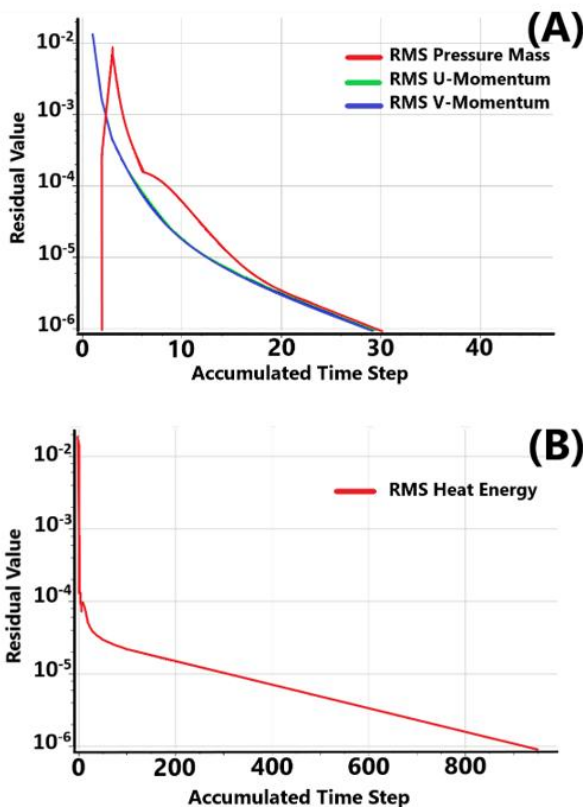


Fig. 3. Residual Convergence for  $Re = 5$ ,  $Ri = 0$ ,  $n = 0.6$  and  $\beta = 0.12$

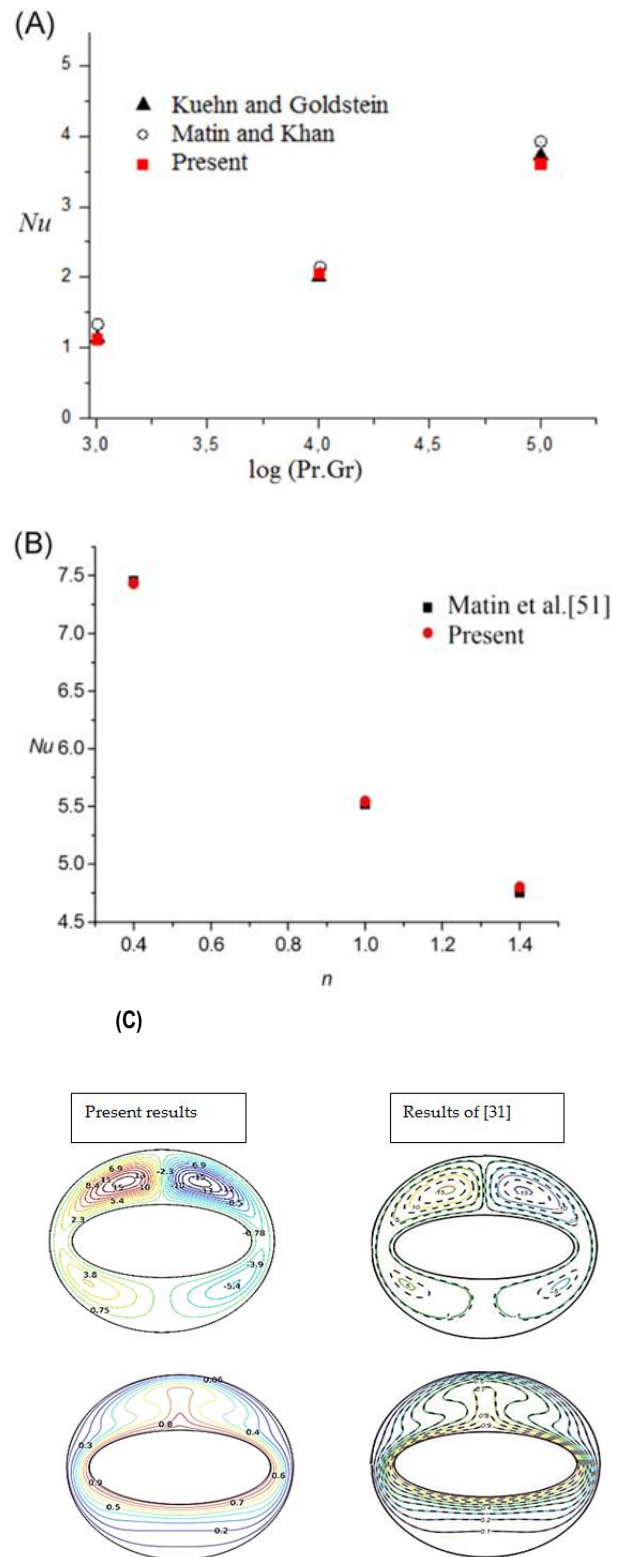


Fig. 4. Validation tests

#### 4. RESULTS AND DISCUSSION

This section provides a detailed presentation and discussion of the streamlines, isotherm contours, and the average Nusselt number for varying values of the power-law index ( $n$ ), Reynolds number ( $Re$ ), and Richardson number ( $Ri$ ).

Three cases are analyzed based on the blockage ratio ( $\beta = d/L$ ): a blockage ratio of 0.12 for the first case, 0.24 for the second, and

0.36 for the third. In each scenario, streamline and isotherm contours illustrate the fluid flow and thermal patterns, respectively.

For the specified governing parameters of  $Ri$  (0, 1, 2, and 3),  $Re$  (1, 5, and 10), and  $n$  (0.6, 1.0, and 1.6) with a fixed  $Pr = 50$ , the Nusselt number ( $Nu$ ) of the inner rotating cylinder is determined. The selected parameter values are based on a previous study [28].

Mixed convection occurs when both forced and natural convection take place simultaneously. In this study, natural convection is

driven by the temperature difference between the inner cylinder and the finned triangular cavity, while forced convection results from the cylinder's rotation. When  $Ri = 0$ , only forced convection is dominant. As the  $Ri$  value increases, the buoyancy force, representing the effect of natural convection, also gradually increases. Meanwhile, the rotational speed is directly related to the Reynolds number ( $Re$ ).

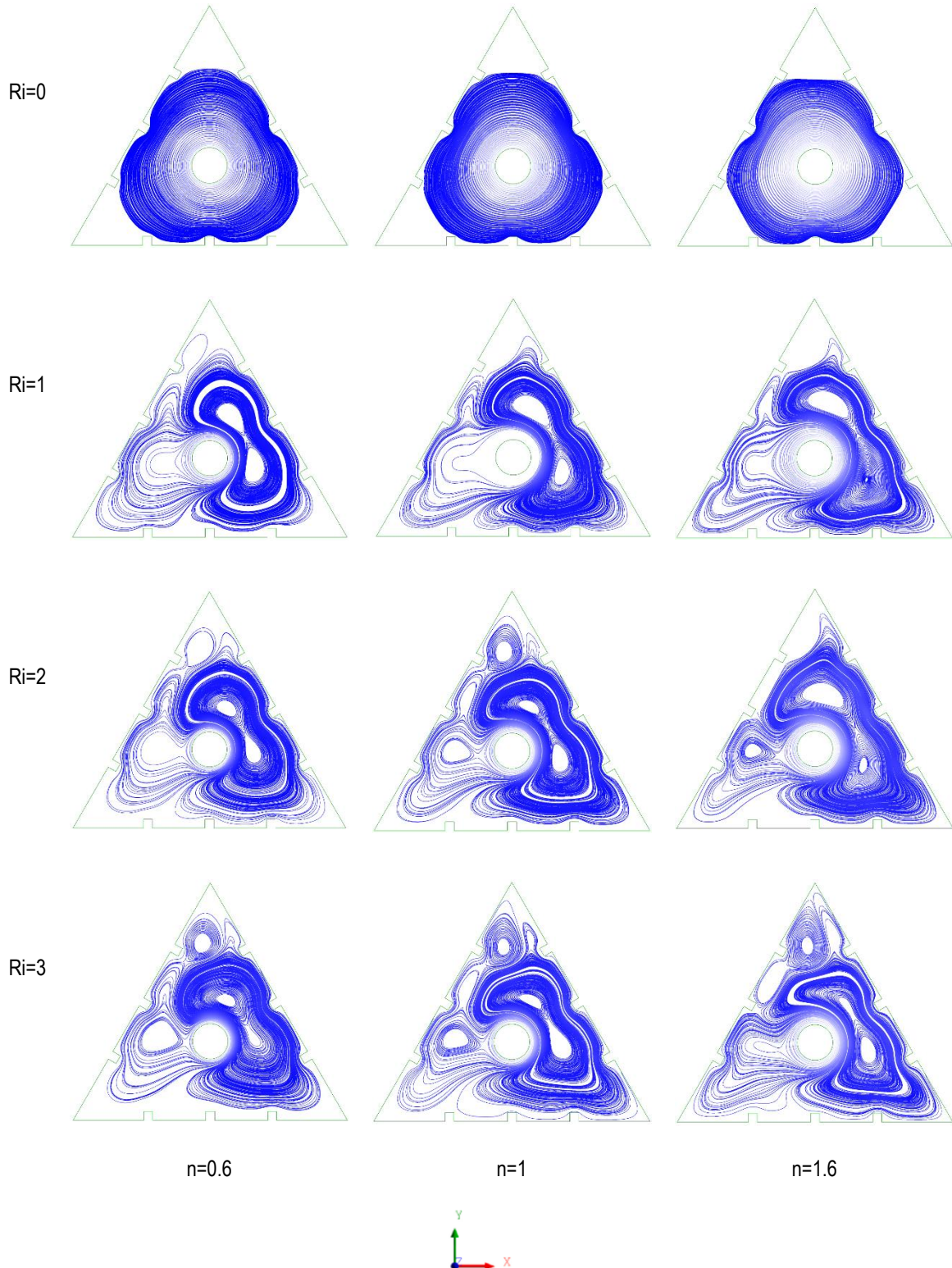


Fig. 5. Streamlines for the case of blockage ratio of 0.12 at  $Re = 5$

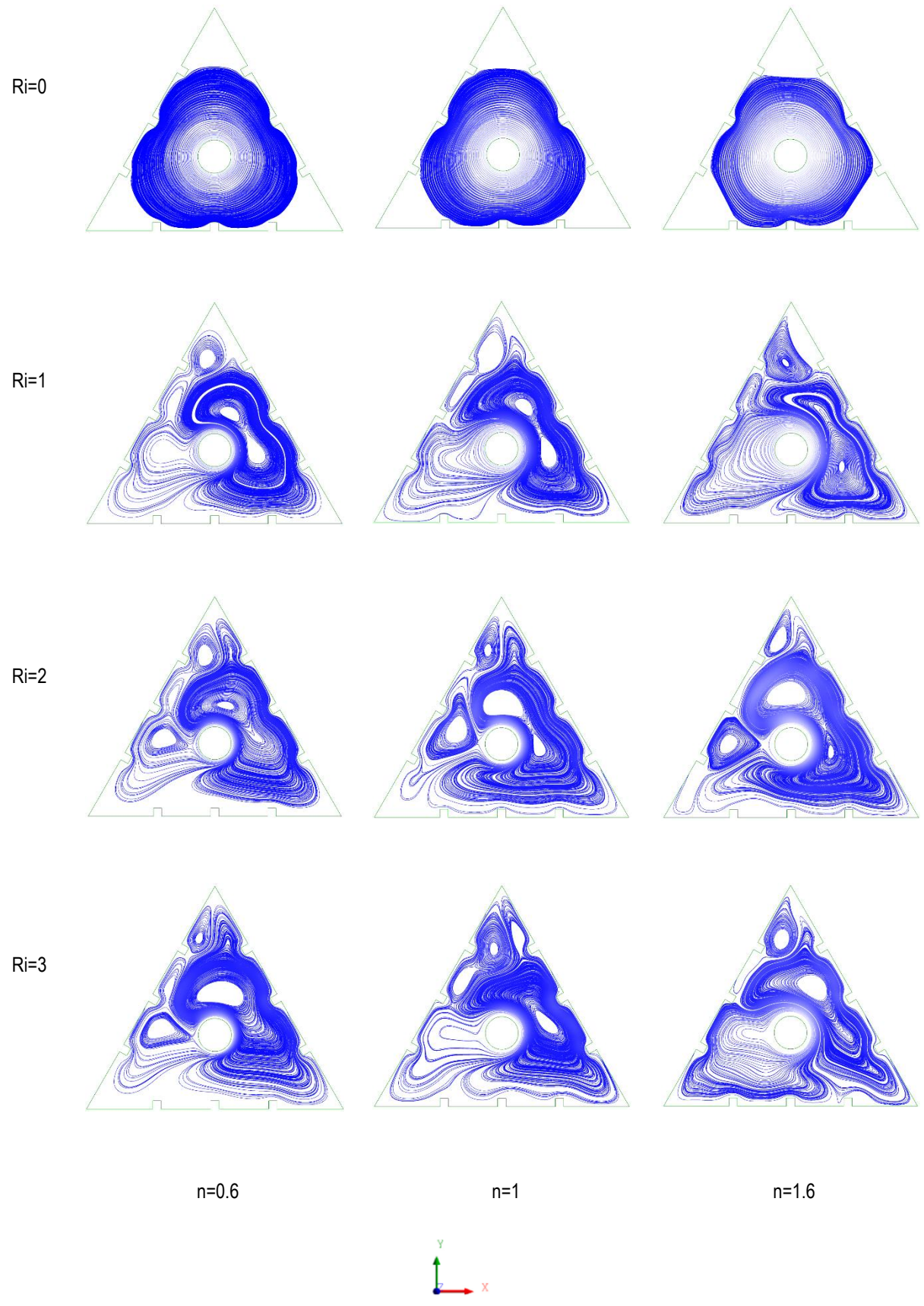


Fig. 6. Streamlines for the case of blockage ratio of 0.12 at  $Re = 10$

**4.1. Case No 1: a blockage ratio of 0.12**

The streamlines in the area between the finned triangular cavity and the inner rotating cylinder are shown in Figs. 5 – 6. In

fact, the streamlines provide a thorough visualization of the particle trajectory and flow fields to identify stagnant and counter-rotating regions. The impact of  $Ri$ ,  $n$ , and  $Re$  on the streamlines is displayed in Figs. 5 – 6.

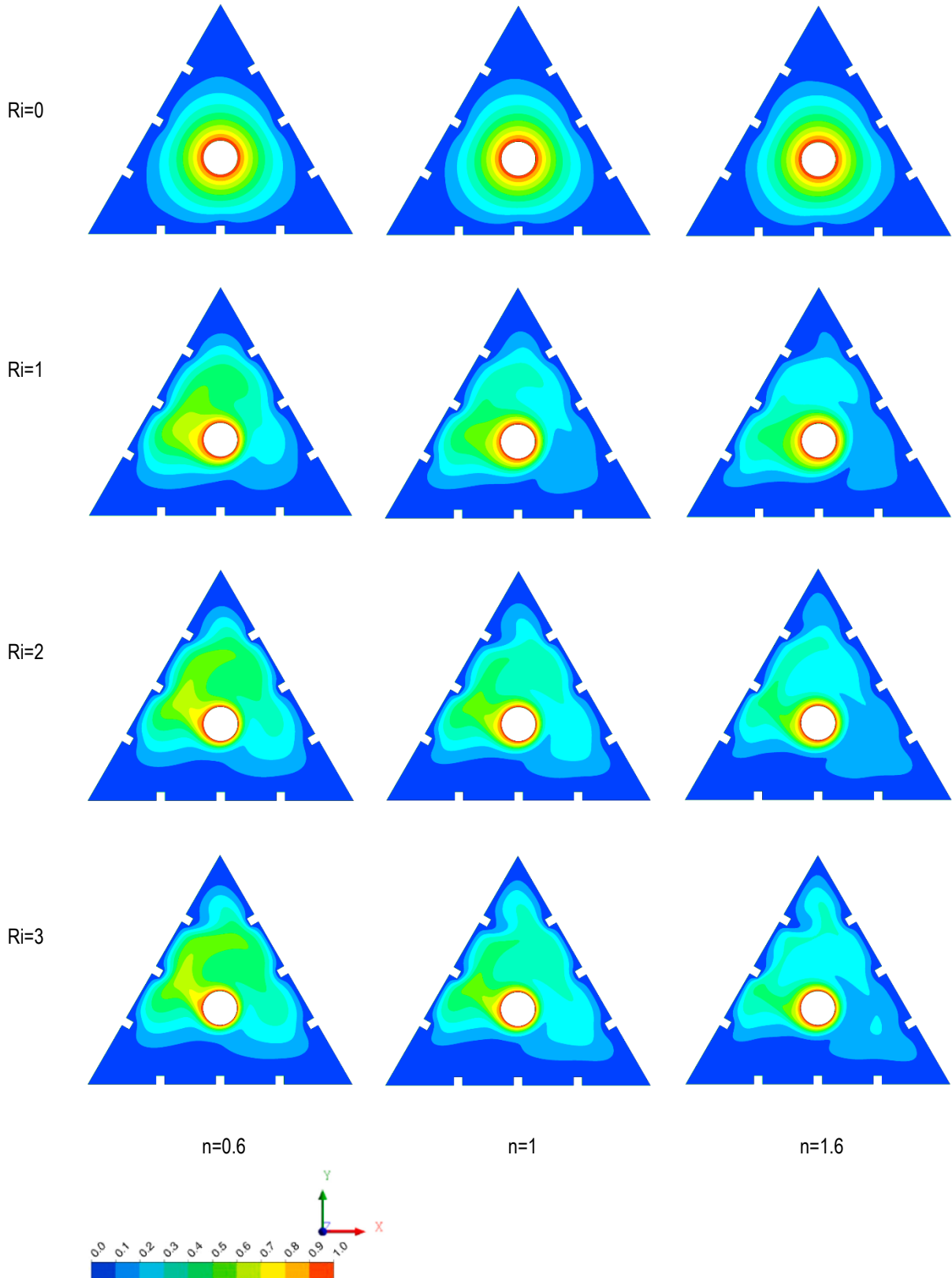


Fig. 7. Isotherms for the case of blockage ratio of 0.12 at  $Re = 5$

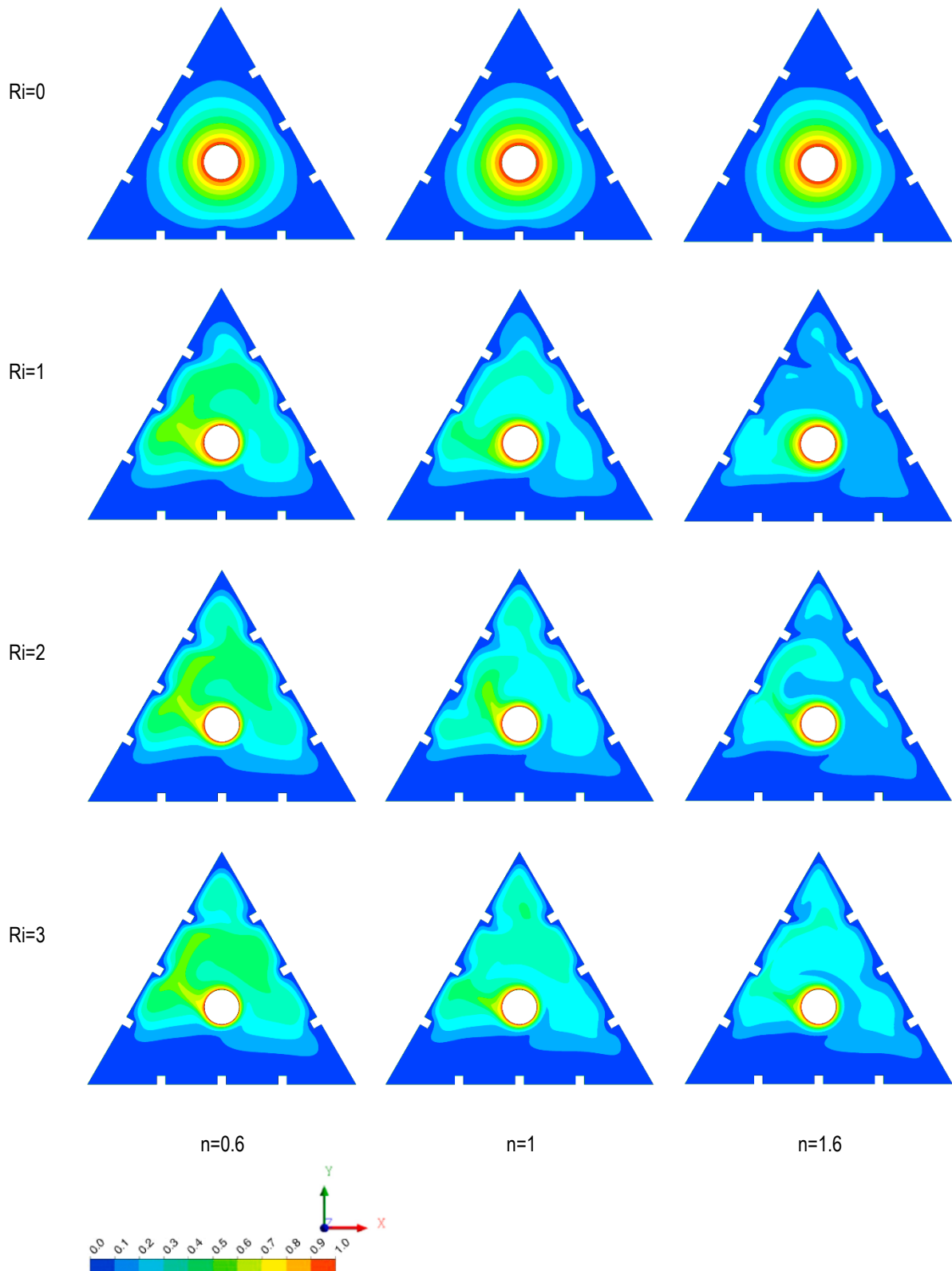


Fig. 8. Isotherms for the case of blockage ratio of 0.12 at  $Re = 10$

Following the rotation of the cylinder ( $\Omega$ ), the flow appears to rotate steadily in the space between the cylinder and the triangular cavity for all values of  $Re$  (5 and 10) and power-law index ( $n = 0.6$ ,

1 and 1.6) for  $Ri = 0$  (pure forced convection). In the mixed convection state ( $Ri \neq 0$ ), a closed counter-rotating region with two loops forms on the right side of the space, while a closed counter-rotating

region with a single loop appears on the left side.

As the Richardson number ( $Ri$ ), representing buoyancy force, and the Reynolds number ( $Re$ ), indicative of rotational speed, increase, the vortex structure on the left side of the domain expands along both the  $x$  and  $y$  axes. In contrast, the two-loop vortex on the right-side contracts with rising values of  $Ri$  and  $Re$ .

Additionally, an increase in the power-law index ( $n$ ) further reduces the overall vortex size. For  $n = 0.6$ , the fluid is shear-thinning, meaning that as shear stress increases, the dynamic viscosity falls. As a result, the fluid particles move easily. On the other hand, when the fluid is shear-thickening ( $n = 1.6$ ), that is, when the dynamic

viscosity increases with the shear stress, the flow becomes more stable. The rotation of the inner cylinder on the right side induces an upward flow of fluid particles, aligning with the direction of the buoyancy force, thus creating a two-loop vortex on the right side of the domain. Conversely, on the left side, the cylinder's rotation counteracts the buoyancy force's influence on fluid particles, resulting in the formation of a single-loop vortex. These observed flow characteristics in the mixed convection regime are fundamentally governed by buoyancy forces, which play a pivotal role in vortex formation.

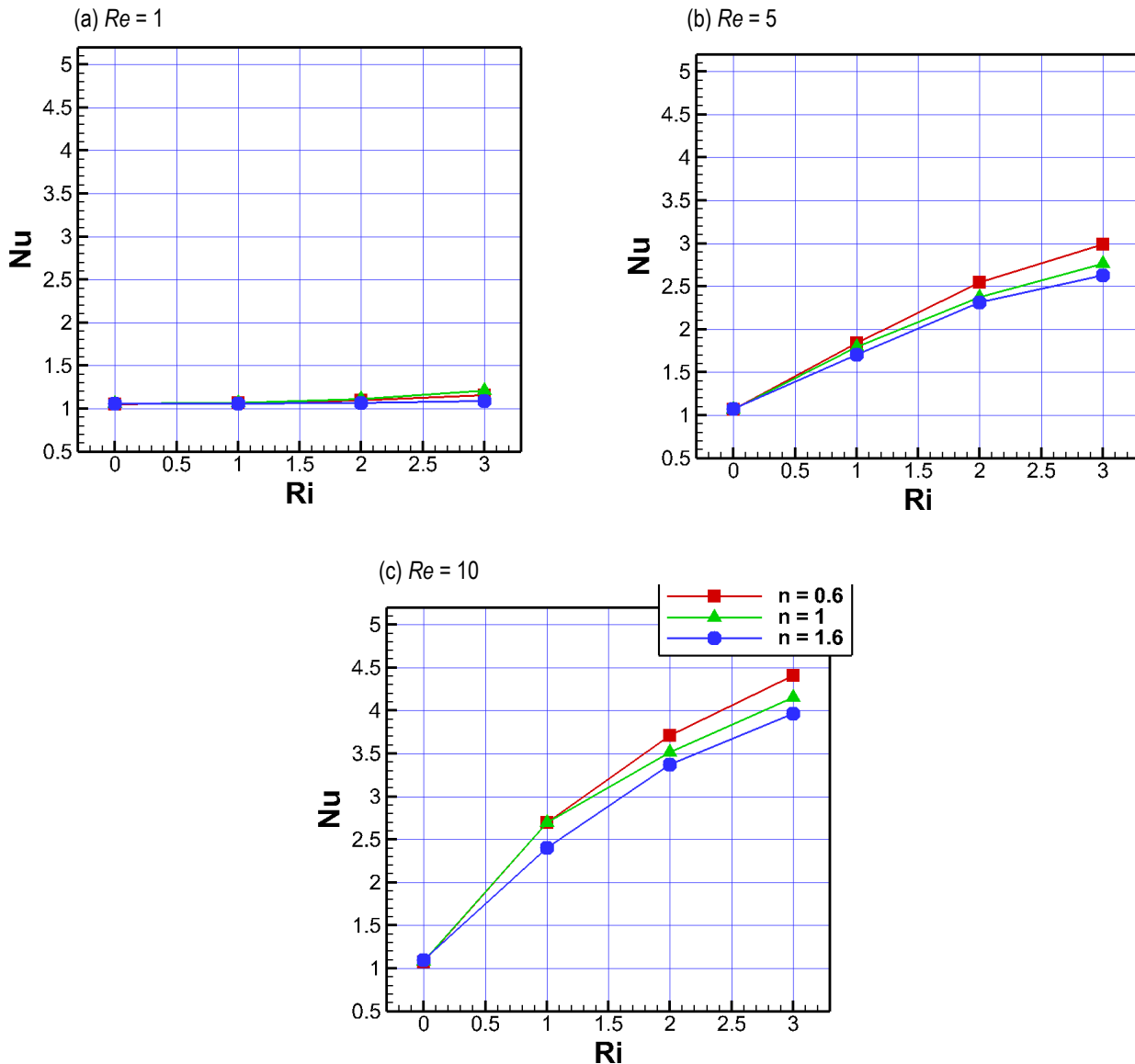


**Fig. 9.** Values of  $Nu$  versus  $Ri$  and  $n$ : a) for  $Re = 1$ ; b)  $Re = 5$ ; and c)  $Re = 10$

The thermal fields in the region between the inner rotating cylinder and the finned triangular cavity are illustrated in Figs. 7 – 8, using the same parameter values for  $n$ ,  $Ri$ , and  $Re$  as in the prior conditions. In the case of  $Ri = 0$ , Figs. 7 – 8 depict a uniform isotherm distribution in all directions. When  $Ri \neq 0$ , however, the thermal distribution aligns with the fluid flow pattern. On the right side,

where the two-loop vortex forms, the cylinder's rotation enhances the thermal buoyancy effect, promoting efficient heat transfer. In contrast, on the left side, fluid recirculation leads to an increase in isotherm thickness near the rotating cylinder. This increase indicates a reduction in the local temperature gradient. Overall, the dimensionless temperature gradient around the triangular block rises with increasing  $Re$  and  $Ri$  but decreases as the power-law index  $n$  increases.

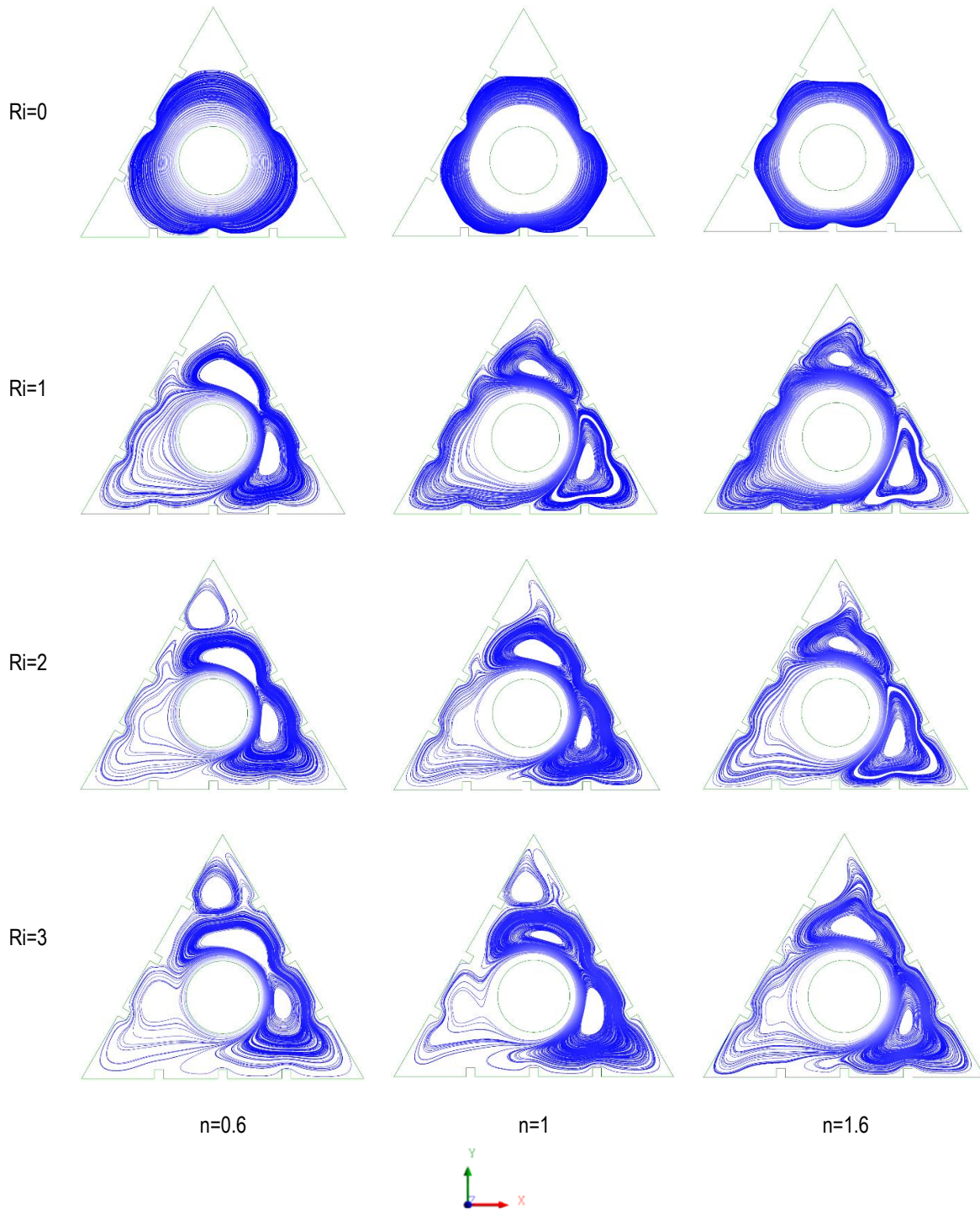


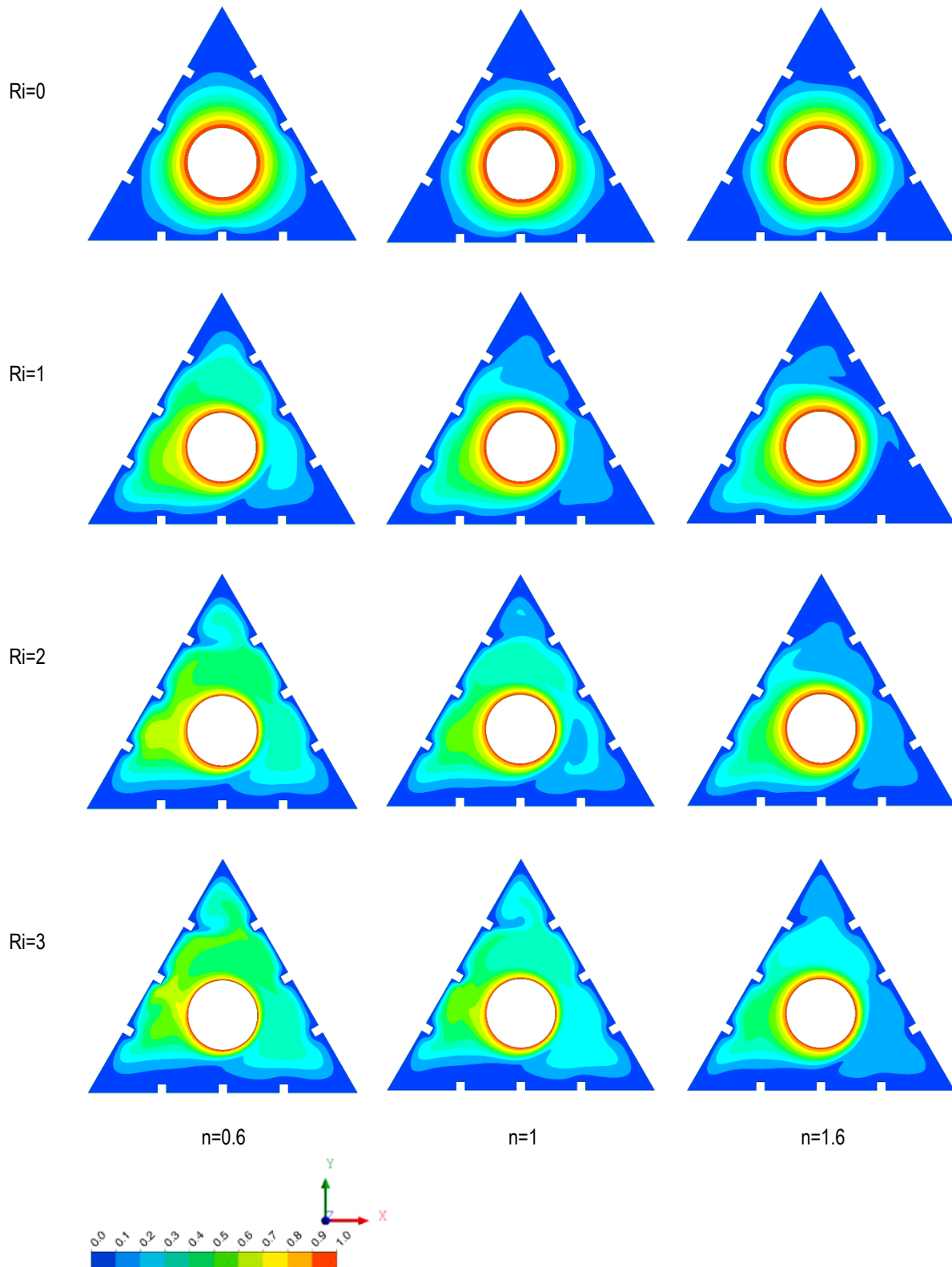
Fig. 10. Streamlines for the case of blockage ratio of 0.24 at  $Re = 10$

Fig. 9 illustrates the variation in the Nusselt number ( $Nu$ ) based on the parameters  $Ri$ ,  $n$ , and  $Re$ . For  $Re=1$ , the effects of the power-law index  $n$  and Richardson number  $Ri$  on  $Nu$  remain minimal due to the low particle velocity, resulting in reduced heat transfer rates. However, at  $Re=5$  and  $Re=10$ , the influence of  $n$  and  $Ri$  becomes more pronounced. As expected,  $Nu$  increases with rising values of  $Re$  and  $Ri$ ; however,  $Nu$  decreases significantly when the fluid behavior shifts from shear-thinning ( $n=0.6$ ) to shear-thickening ( $n=1.6$ ). This reduction occurs because the increased viscosity of the dilatant (shear-thickening) fluid restricts the development of the thermal boundary layer, impeding the temperature gradient,

experimental observations [30] are in agreement with our findings.

#### 4.2. Case No 2: a blockage ratio of 0.24

In this case, the ratio of the cylinder diameter  $d$  to the side length of the triangular cavity  $L$  is set to 0.24. Fig. 10 illustrates the effects of the Richardson number  $Ri$  and the power-law index  $n$  on the streamlines at  $Re = 10$ . For all values of  $Ri$  and  $n$ , the streamlines closely resemble those in the initial case, with vortices growing on both the right and left sides of the domain under mixed convection conditions ( $Ri \neq 0$ ).



**Fig. 11.** Isotherms for the case of blockage ratio of 0.24 at  $Re = 10$

The isotherms of the second case are shown in Fig. 11, the results indicate an increase in the isotherm thicknesses around the rotating cylinder for  $Ri \neq 0$  due to the vortices growth of fluid molecules.

The estimated values of  $Nu$  versus  $Ri$ ,  $n$ , and  $Re$  for the second case are shown in Fig. 12. The effects of the Richardson number ( $Ri$ ) and the power law index ( $n$ ) on  $Nu$  for all  $Re$  values are consistent with the findings of the first case, with  $Nu$  values reducing by approximately 30%.

### 4.3. Case No 3: a blockage ratio of 0.36

In this case, the blockage ratio ( $\beta=d/L$ ) is set to 0.36. Fig. 13 illustrates the streamlines for various values of  $Ri$  and  $n$  at  $Re=10$ . The streamlines depicted in this figure differ from those observed in earlier cases, as spaced vortices emerge in the corners of the

triangular cavity. Additionally, the counter-rotational loops are smaller compared to those in previous cases under mixed convection conditions ( $Ri \neq 0$ ). This reduction in size is attributed to the contraction of the fluid area resulting from the increased dimensions of the inner cylinder.

The isotherms for this case are illustrated in Fig. 14, which indicates a reduction in the thickness of the isotherms surrounding the rotating cylinder for  $Ri \neq 0$  in comparison to the previous two cases. This phenomenon can be attributed to the development of the streamlines discussed earlier.

The values of the Nusselt number ( $Nu$ ) for this case, considering  $Ri$ ,  $n$ , and  $Re$ , are presented in Fig. 15. Both  $Re$  and  $Ri$  positively influence  $Nu$ . In the context of pseudoplastic fluids, the relationships between  $Nu$  and the parameters  $Re$  and  $Ri$  are significant, particularly when the viscosity is at its minimum. Notably, the  $Nu$  values in this case are lower than those observed in the previous cases.

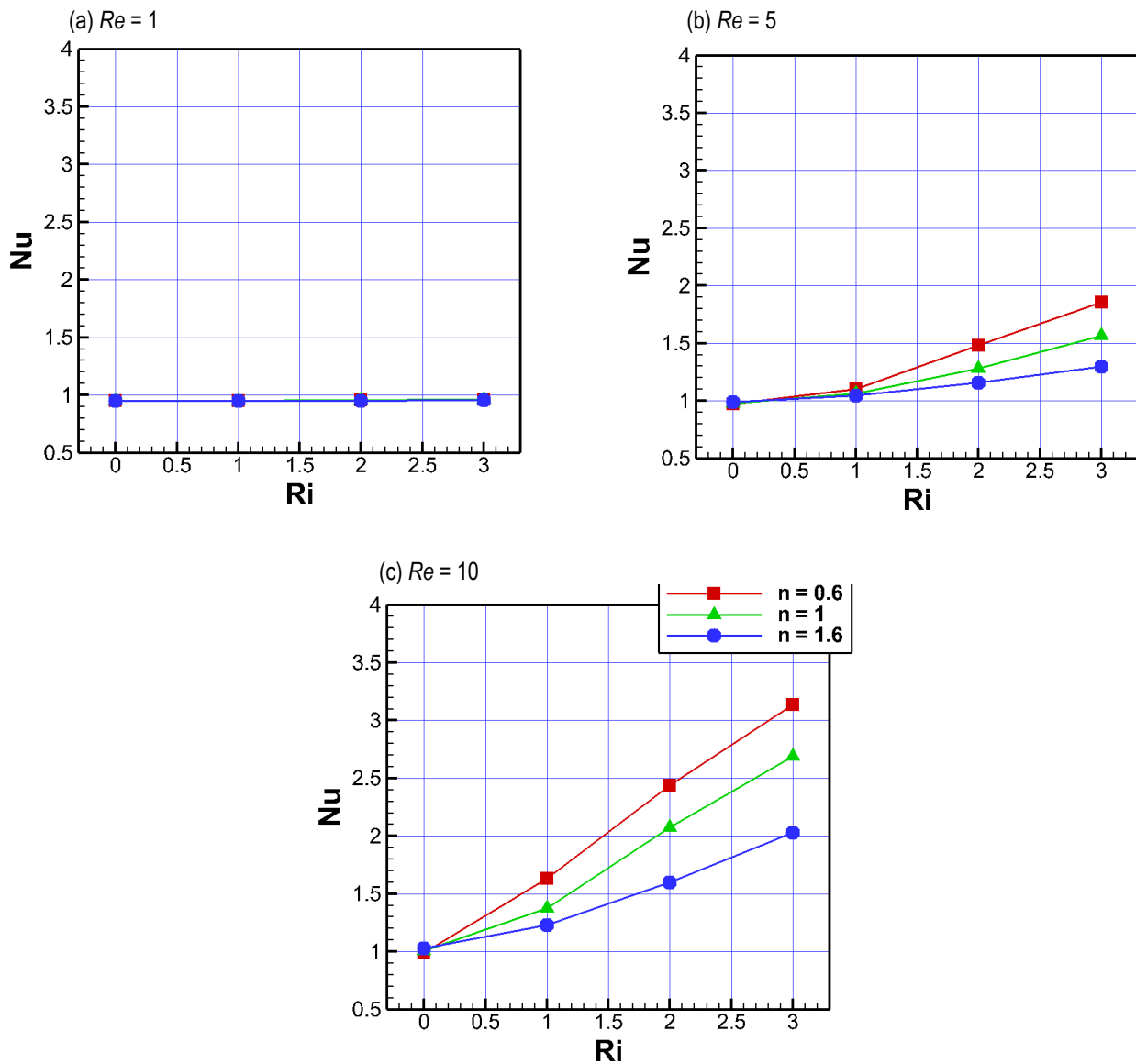


Fig. 12. Values of  $Nu$  versus  $Ri$  and  $n$ : a) for  $Re = 1$ ; b)  $Re = 5$ ; and c)  $Re = 10$

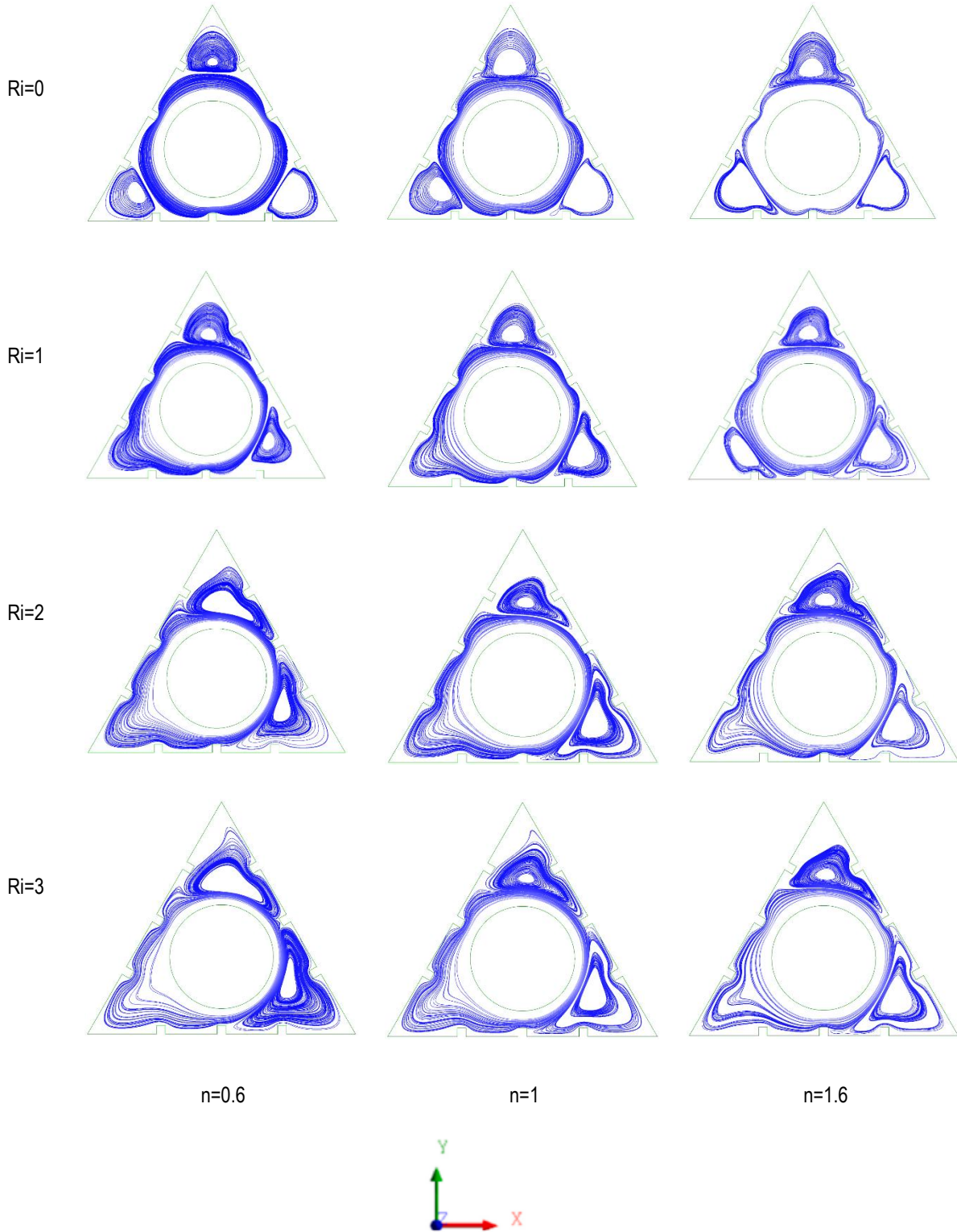
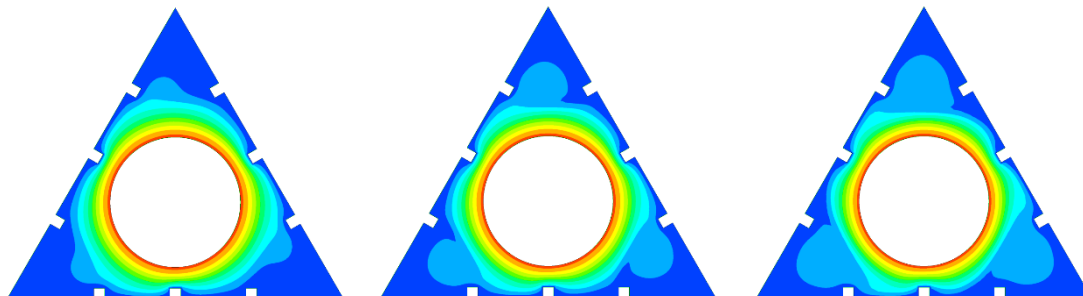


Fig. 13. Streamlines for the case of blockage ratio of 0.36 at  $Re = 10$

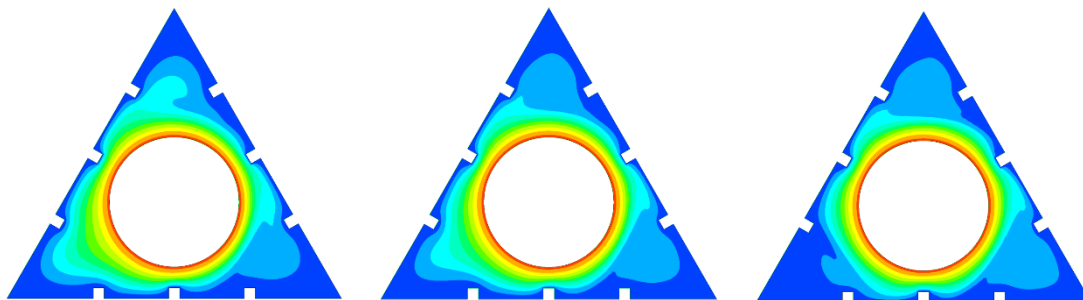
Fig. 16 presents a comparison of the Nusselt number ( $Nu$ ) values for the three cases examined as a function of the Richardson number ( $Ri$ ). The selected parameters are  $n=0.6$  and  $Re=10$ . It is clear that in the mixed convection scenario involving power-law fluids, the heat transfer rate decreases significantly and progressively

from the initial state to the final state. These observations are consistent with a previous result [29], which show that higher blockage ratios stabilize the fluid flow and reduce the overall heat transfer rate.

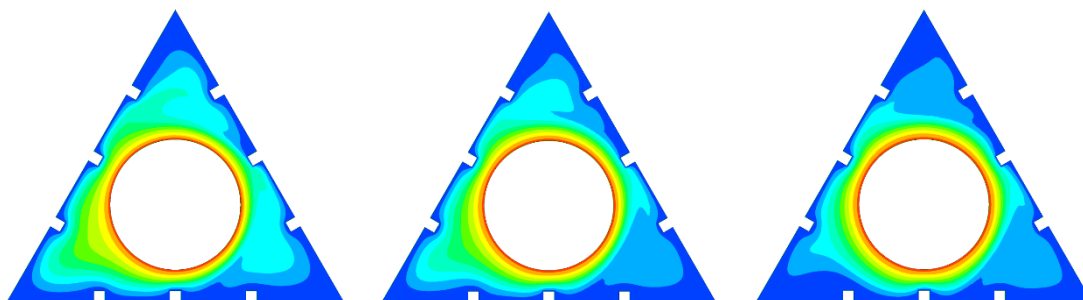
Ri=0



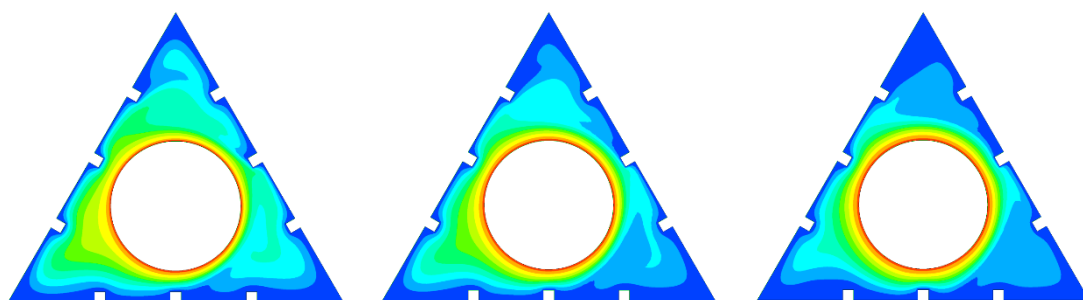
Ri=1



Ri=2



Ri=3



n=0.6

n=1

n=1.6

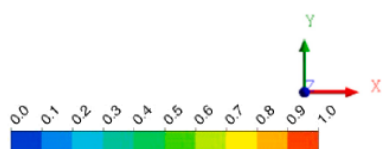


Fig. 14. Isotherms for the case of blockage ratio of 0.36 at  $Re = 10$

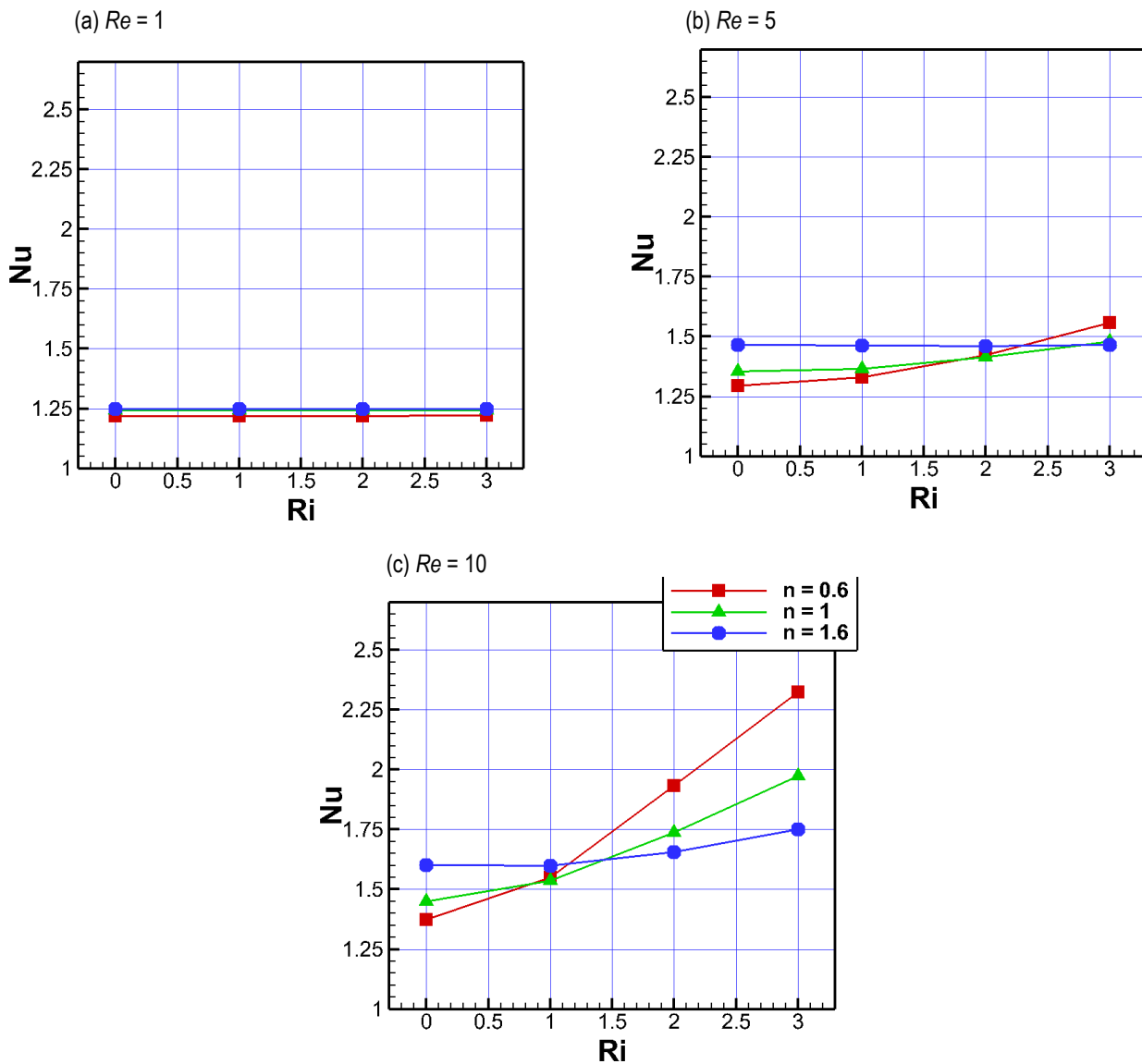


Fig. 15. Values of  $Nu$  versus  $Ri$  and  $n$ : a) for  $Re = 1$ ; b)  $Re = 5$ ; and c)  $Re = 10$

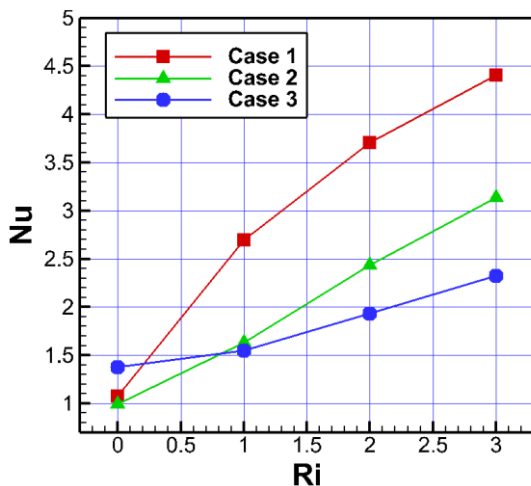


Fig. 16. Values of  $Nu$  with  $Ri$  for the three cases at  $Re = 10$  and  $n = 0.6$

## 5. CONCLUSION

This paper presents a numerical study on the behavior of a non-Newtonian fluid in a finned triangular cavity with a rotating, high-temperature horizontal cylinder. The cavity walls are maintained at a cold temperature. The study examines the effects of key parameters, including the power-law index ( $n$ ), Reynolds number ( $Re$ ), blockage ratio ( $\beta$ ), and Richardson number ( $Ri$ ), on fluid flow and thermal activity. The main findings are as follows:

- Increasing the blockage ratio stabilizes the flow by reducing disturbances and counter-rotating zones, but it also decreases the overall heat transfer rate;
- Higher thermal buoyancy promotes recirculation zones and vertical fluid motion, increasing the thermal activity around the heated cylinder;
- A higher Reynolds number enhances flow velocity and heat transfer due to increased rotational speed;

- A larger power-law index ( $n$ ) increases fluid viscosity, reducing flow velocity and thermal activity;
- Shear-thickening fluids with a high blockage ratio are suited for thermal insulation, while shear-thinning fluids with a low blockage ratio are ideal for cooling.

#### Nomenclature

A	Surface area of the inner cylinder, $m^2$
$C_p$	Heat capacity of fluid, $J\ kg^{-1}\ K^{-1}$
$d$	Diameter of the inner cylinder, $m$
L	Side length of the triangular cavity, $m$
Gr	Grashof number
g	Gravitational acceleration, $m\ s^{-2}$
$I_2$	Second invariant function of strain rate tensor
K	Thermal conductivity of fluid, $W\ m^{-1}\ K^{-1}$
m	Consistency index, $Pa\ s^n$
Nu	Nusselt number (average value)
$Nu_L$	Nusselt number (local value)
n	Power-law index
$Pr$	Prandtl number
p	Pressure, Pa
Re	Reynolds number
Ri	Richardson number
T	Temperature, K
u, v	Velocity components along x and y directions, $m\ s^{-1}$
x, y	Cartesian coordinates, m

#### Greek symbols

$\beta$	Blockage ratio
$\beta_T$	Coefficient of volume expansion
$\eta$	Dynamic viscosity, Pa s
$\rho$	Density of fluid, $kg\ m^{-3}$
$\tau$	Stress tensor, Pa
$\Omega$	Rotation speed, $1/s$

#### Subscripts/Superscripts

c	Cold
h	Hot
*	dimensionless quantity

#### REFERENCES

1. Mishra L, Baranwal A, Chhabra R, Laminar forced convection in power-law fluids from two heated cylinders in a square duct, International Journal of Heat and Mass Transfer. 2017; 113 :589–612. <https://doi.org/10.1016/j.ijheatmasstransfer.2017.05.117>
2. Mohebbi R, Delouei A, Jamali A, Izadi M, Mohamad A, Pore-scale simulation of non-Newtonian power-law fluid flow and forced convection in partially porous media: Thermal lattice Boltzmann method, Physica A. 2019; 525 :642–656. <https://doi.org/10.1016/j.physa.2019.03.039>
3. Malkeson S, Alshaailli S, Chakraborty N, Numerical investigation of steady state laminar natural convection of power-law fluids in sidecooled trapezoidal enclosures heated from the bottom, Numerical Heat Transfer, Part A: Applications. 2023; 83 :770–789. <https://doi.org/10.1080/10407782.2022.2157353>
4. Rashid U, Shahzad H, Lu D, Wang X, Majeed A, Non-Newtonian MHD double diffusive natural convection flow and heat transfer in a crown enclosure, Case Studies in Thermal Engineering. 2023; 41:102541. <https://doi.org/10.1016/j.csite.2022.102541>
5. Lamsaadi M, Naimi M, Hasnaoui M, Natural convection of non-Newtonian power law fluids in a shallow horizontal rectangular cavity uniformly heated from below, Heat Mass Transfer. 2005; 41 :239–249. <http://dx.doi.org/10.1007/s00231-004-0530-8>
6. Lamsaadi M, Naimi M, Hasnaoui M, Mamou M, Natural Convection in a Vertical Rectangular Cavity Filled with a Non-Newtonian Power Law Fluid and Subjected to a Horizontal Temperature Gradient, Numerical Heat Transfer, Part A.2006;49:969–990. <http://dx.doi.org/10.1080/10407780500324988>
7. Mahmood F, Chowdhury T, Hasan M, Fluid-structure interaction induced mixed convection characteristics in a lid-driven square cavity with non-Newtonian power law fluids, International Journal of Thermofluids. 2024; 22:100687. <https://doi.org/10.1016/j.ijft.2024.100687>
8. Bilal S, Khan N, Fatima I, Riaz A, Ansari G, Alhazmi S, Tag El-Din E, Mixed convective heat transfer in a power-law fluid in a square enclosure: Higher order finite element solutions, Frontiers in Physics.2022; 10 :1079641. <http://dx.doi.org/10.3389/fphy.2022.1079641>
9. Roy P, Chowdhury S, Raj M, Islam M, Saha S, Forced, natural and mixed convection of Non-Newtonian fluid flows in a square chamber with moving lid and discrete bottom heating, Results in Engineering. 2023; 17 :100939. <http://dx.doi.org/10.1016/j.rineng.2023.100939>
10. Prasad D, Chaitanya G, Raju R, Double diffusive effects on mixed convection Casson fluid flow past a wavy inclined plate in presence of Darcian porous medium, Results in Engineering. 2019; 3 :100019. <http://dx.doi.org/10.1016/j.rineng.2019.100019>
11. Thohura S, Molla M, Sarker M, Paul M, Study of mixed convection flow of power-law fluids in a skewed lid-driven cavity, Heat Transfer. 2021;10:1–30. <http://dx.doi.org/10.1002/htj.22174>
12. Hussain S, Jamal M, Geridonmez B, Impact of power law fluid and magnetic field on double diffusive mixed convection in staggered porous cavity considering Dufour and Soret effects, International Communications in Heat and Mass Transfer. 2021;121:105075. <http://dx.doi.org/10.1016/j.icheatmasstransfer.2020.105075>
13. Laidoudi H, Natural convection from four circular cylinders in across arrangement within horizontal annular space, Acta Mechanica et Automatica. 2020;14:98-102. <http://dx.doi.org/10.2478/ama-2020-0014>
14. Laidoudi H, Abderrahmane A, Saeed A. M, Guedri K, Weera W, Younis O, Mourad A, Marzouki R, Irreversibility interpretation and MHD mixed convection of hybrid nanofluids in a 3D heated lid-driven chamber, Nanomaterials. 2022;12:1747. <https://doi.org/10.3390/nano12101747>
15. Laidoudi H, Bouziti M, Mixed convection heat transfer from confined tandem circular cylinders in cross-flow at low Reynolds number. Mechanics. 2017; 23: 522-527. <https://doi.org/10.5755/j01.mech.23.4.15258>
16. Acharya N, Framing the effect of fitted curved fins' curvature on the flow patterns and entropy analysis of buoyancy-driven magnetized hybrid nanofluidic transport within an annular enclosure, Journal of Energy Storage.2024; 100: 113638. <https://doi.org/10.1016/j.est.2024.113638>
17. Acharya N, Magnetically driven MWCNT-Fe3O4-water hybrid nanofluidic transport through a micro-wavy channel: a novel MEMS design for drug delivery application. Materials Today Communications. 2024; 38:107844. <https://doi.org/10.1016/j.mtcomm.2023.107844>
18. Acharya N, Hydrothermal scenario of buoyancy-driven magnetized multi-walled carbon nanotube-Fe3O4-water hybrid nanofluid flow within a discretely heated circular chamber fitted with fins. Journal of Magnetism and Magnetic Materials. 2024; 589:171612. <https://doi.org/10.1016/j.jmmm.2023.171612>
19. Acharya N, On the magnetohydrodynamic natural convective alumina nanofluidic transport inside a triangular enclosure fitted with fins. Journal of the Indian Chemical Society. 2022; 99(12): 100784. <https://doi.org/10.1016/j.jics.2022.100784>
20. Acharya N, Effects of different thermal modes of obstacles on the natural convective Al2O3-water nanofluidic transport inside a triangular

- cavity. Proceedings of the Institution of Mechanical Engineers, Part C: Journal of Mechanical Engineering Science. 2022; 236(10): 5282-99.  
<http://dx.doi.org/10.1177/09544062211061484>
21. Acharya N, Buoyancy driven magnetohydrodynamic hybrid nanofluid flow within a circular enclosure fitted with fins. International Communications in Heat and Mass Transfer. 2022; 133: 105980.  
<https://doi.org/10.1016/j.icheatmasstransfer.2022.105980>
  22. Tayebi T, Dogonchi AS, Karimi N, Ge-JiLe H, Chamkha AJ, Elmasry Y. Thermo-economic and entropy generation analyses of magnetic natural convective flow in a nanofluid-filled annular enclosure fitted with fins, Sustain. Energy Technol. Assess. 2021; 46:1–30./  
<https://doi.org/10.1016/j.seta.2021.101274>
  23. Chamkha AJ, Dogonchi AS, Ganji DD. Magnetohydrodynamic nanofluid natural convection in a cavity under thermal radiation and shape factor of nanoparticles impacts: a numerical study using CVFEM. Applied Sciences. 2018 Nov 26;8(12):2396.  
<https://doi.org/10.3390/app8122396>
  24. Seyyedi SM, Dogonchi AS, Hashemi-Tilehnoee M, Ganji DD, Chamkha AJ. Second law analysis of magneto-natural convection in a nanofluid filled wavy-hexagonal porous enclosure. International Journal of Numerical Methods for Heat & Fluid Flow. 2020; 30: 4811-36.  
<https://doi.org/10.1108/HFF-11-2019-0845>
  25. Dogonchi AS, Waqas M, Afshar SR, Seyyedi SM, Hashemi-Tilehnoee M, Chamkha AJ, Ganji DD. Investigation of magnetohydrodynamic fluid squeezed between two parallel disks by considering Joule heating, thermal radiation, and adding different nanoparticles. International Journal of Numerical Methods for Heat & Fluid Flow. 2020; 30:659-80. <https://doi.org/10.1108/HFF-05-2019-0390>
  26. Eshaghi S, Izadpanah F, Dogonchi AS, Chamkha AJ, Hamida MB, Alhumade H. The optimum double diffusive natural convection heat transfer in H-Shaped cavity with a baffle inside and a corrugated wall. Case Studies in Thermal Engineering. 2021; 28: 101541.  
<https://doi.org/10.1016/j.csite.2021.101541>
  27. Abu-Ghurban M, Al-Farhany K. Mixed convective heat transfer in an open cavity with fins. Heat Transfer. 2024; 53(8): 4169-96.  
<https://doi.org/10.1002/htj.23128>
  28. Laidoudi H, Ameer H, Investigation of the mixed convection of power-law fluids between two horizontal concentric cylinders: Effect of various operating conditions, New Journal and we have not received input yet. 2020; 20:100731.  
<http://dx.doi.org/10.1016/j.tsep.2020.100731>
  29. Salman Z, Aiss F, Almudhaffar M. Experimental study of mixed convection in a cavity with a rotating cylinder. Journal of Advanced Research in Fluid Mechanics and Thermal Sciences. 2020; 74:16-26.  
<https://doi.org/10.37934/arfmts.74.2.1626>
  30. Chun S, Ji B, Yang Z, Malik VK, Feng J. Experimental observation of a confined bubble moving in shear-thinning fluids. Journal of Fluid Mechanics. 2022; 953: A12.  
<https://doi.org/10.1017/jfm.2022.926>
  31. Sheikholeslami M. CuO-water nanofluid free convection in a porous cavity considering Darcy law. European Physical Journal Plus. 2017; 132: 55.  
<https://doi.org/10.1140/epjp/i2017-11330-3>

Youcef Lakahal:  <https://orcid.org/0009-0005-7444-4880>

Houssein Laidoudi:  <https://orcid.org/0000-0001-8700-7077>



This work is licensed under the Creative Commons BY-NC-ND 4.0 license.